



Hydrogen spillover in MoO_xRh hierarchical nanosheets boosts alkaline HER catalytic activity

Shuyuan Pan^{a,b}, Chen Li^{a,*}, Tiantian Xiong^b, Yuhua Xie^b, Fang Luo^{a,*}, Zehui Yang^{b,*}

^a College of Materials Science and Engineering, State Key Laboratory of New Textile Materials & Advanced Processing Technology, Wuhan Textile University, Wuhan 430200, PR China

^b Hydrogen Energy Technology Innovation Center of Hubei Province, Faculty of Materials Science and Chemistry, China University of Geosciences Wuhan, 388 Lumo RD, Wuhan 430074, PR China

ARTICLE INFO

Keywords:

Hydrogen evolution reaction
Molybdenum oxide
Rhodium hierarchical nanosheets
Hydrogen spillover
Water dissociation

ABSTRACT

The low intrinsic catalytic performance and stability are the two dominant obstacles for alkaline hydrogen evolution reaction (HER) electrocatalyst. Herein, amorphous molybdenum oxide (MoO_x) has been introduced to rhodium hierarchical nanosheets (MoO_xRh-HNS) at atomic level efficiently reducing the barrier for hydrogen spillover from Rh to MoO_x; thereby, MoO_xRh-HNS exhibit superior HER activity with mass activity of 23.9 A mg_{noble metal}⁻¹ at overpotential of 200 mV, which is boosted by 10.8- and 14.9-fold with relative to Rh-HNS and Pt/C in alkaline media, respectively. Meanwhile, Tafel slope is as low as 22.5 mV dec⁻¹ for MoO_xRh-HNS revealing a hydrogen-spillover-involving HER mechanism proved by the electrochemical test as well as operando electrochemical impedance spectroscopy. Density functional theory calculation indicates the adsorbed hydrogen on MoO_xRh promotes the water dissociation and balances the hydrogen binding strength to a moderate level. Simultaneously, the hierarchical nanosheet structure contributes a robust HER stability at 500 mA cm⁻². This work offers a new methodology to construct a high-performance alkaline HER electrocatalyst with industrial-level current density.

1. Introduction

Electrochemical splitting of H₂O to generate hydrogen is a valid methodology to store the intermittent energies; therefore, the unbalanced energy distribution can be well resolved [1–4]. For alkaline water splitting technology, more attention should be paid to hydrogen evolution reaction (HER), an uphill reaction normally driven by platinum (Pt) [5–7]. The industrialization of alkaline water splitting technology predominantly depends on the HER electrocatalyst with excellent catalytic performance and stability since alkaline HER catalysis is sluggish due to its primary water dissociation step to generate atomic hydrogen [8–10]. Although, numerous investigations on transition metal-based phosphides [5,11], nitrides [12,13], sulfides [14,15], and carbides [16,17] have been reported as robust HER electrocatalysts; however, noble metals are still considered as the Holy Grail for alkaline HER catalysis [18–20]. Nevertheless, it is necessary to further boost the intrinsic catalytic performance toward alkaline HER catalysis [21,22].

Tremendous effects have been made to manufacture noble metal based electrocatalyst, such as, size controlling [23–25], morphology

adjustment [26,27], engineering in crystal phase [28], introduction of secondary component [29,30], etc. Recently, hybridizing noble metal with another component to improve HER performance via hydrogen spillover has been reported to surmount the restriction of Sabatier's principle, in which an efficient HER electrocatalyst should perform a moderate binding strength with hydrogen [31]. A hydrogen enriched noble metal atom accompanied with hydrogen deficient components as second phase or supports (WO_{3-x} [32], SiNW [33], MoS₂ [34], CoP [35], etc.) composed of the hydrogen spillover electrocatalyst. Hydrogen firstly adsorbed on noble metal atom and diffused to adjacent hydrogen deficient component; therefore, H₂ desorption could occur on the noble metal atom as well as the support or secondary phase. While, the hydrogen spillover process is constrained by the far reaction path associated with interfacial resistance between two components, like unmatched lattice spacing and Schottky barrier [36,37]. Therefore, construction of interface-free and shortening the reaction path at atomic level are efficient methodologies to accelerate the hydrogen spillover process. Amorphous structure with long range disorder possesses comparably lower diffusion barrier than crystal [38,39]. As a

* Corresponding authors.

E-mail addresses: cli@wtu.edu.cn (C. Li), luofang04@gmail.com (F. Luo), yeungzehui@gmail.com (Z. Yang).

<https://doi.org/10.1016/j.apcatb.2023.123275>

Received 20 June 2023; Received in revised form 21 August 2023; Accepted 6 September 2023

Available online 7 September 2023

0926-3373/© 2023 Elsevier B.V. All rights reserved.

consequence, introduction of amorphous transition metal oxides to the neighboring noble metal atoms could promote the hydrogen spillover; thereby, a superior HER electrocatalyst is acquired [40].

Considering the above analysis, in this work, we have synthesized Rh hierarchical nanosheets incorporated by amorphous molybdenum oxide ($\text{MoO}_x\text{Rh-HNS}$) at atomic level. With the introduction of MoO_x , $\text{MoO}_x\text{Rh-HNS}$ performed an exceptional HER catalytic performance and a low Tafel slope of 22.5 mV dec^{-1} in alkaline electrolyte requiring only 102.5 mV overpotential to attain 200 mA cm^{-2} , decreased by 283.5 mV and 233.5 mV by comparison with Pt/C and Rh-HNS due to the occurrence of hydrogen spillover during HER catalysis supported by electrochemical experiments. With the adsorption of hydrogen on $\text{MoO}_x\text{Rh-HNS}$, the water dissociation (Volmer reaction) was more prone to occur and the overly strong binding strength with hydrogen was simultaneously loosened. This work opens a new avenue to manufacture a high-performance HER electrocatalyst in alkaline medium.

2. Experimental section

Materials and chemicals: Rhodium acetylacetonate ($\text{Rh}(\text{acac})_3$, 97 %), molybdenum (VI) dioxide bis(acetylacetonate) ($\text{MoO}_2(\text{acac})_2$, 97 %), formaldehyde (37 wt% in H_2O), carbon black (Vulcan XC-72) and Nafion solution D520 (5 wt%) were purchased from Alfa Aesar.

Synthesis of $\text{MoO}_x\text{Rh-HNS}$: In a 50 mL beaker, 20 mg of $\text{Rh}(\text{acac})_3$, $\text{MoO}_2(\text{acac})_2$ and 8 mL ultrapure water were added and stirred for 0.5 h at 25°C . Then 4 mL of formaldehyde was added. The solution was added to a stainless autoclave lined with Teflon and heated from room temperature to 180°C kept for 10 h. After the autoclave was cooled to 25°C , the product was washed with ethanol for more than three times to remove organic matter, and then dried in a vacuum oven at 65°C for 10 h. MoO_x was obtained without the addition of a rhodium source. With the same amount of rhodium source, 0 mg, 8.5 mg, 17 mg, 34 mg of $\text{MoO}_2(\text{acac})_2$ was added, respectively. The product and XC-72 were mixed and sonicated in ethanol for 30 min, and the resulting substances were named Rh-HNS , $\text{MoO}_x\text{Rh-HNS-1}$, $\text{MoO}_x\text{Rh-HNS-2}$, $\text{MoO}_x\text{Rh-HNS-3}$, respectively.

3, respectively.

3. Results and discussion

3.1. Fundamental characterizations

The component in the as-prepared electrocatalysts were detected by XRD technology. As shown in Fig. 1a, a broad peak at 25° was observed ascribed to the graphitic carbon (002) plane ascribed to the presence of carbon black. For $\text{MoO}_x\text{Rh-HNS-2}$ and Rh-HNS , a sharp diffraction peak at 41° was detected revealing the formation of metallic Rh in two electrocatalysts according to JCPDS: PDF#01-1214 since this peak was the signal of dominant (111) facet. Similar XRD pattern was found for Rh-HNS and $\text{MoO}_x\text{Rh-HNS-2}$ indicating the introduction of Mo precursor negligibly affect the phase information, also evidenced by the XRD patterns of $\text{MoO}_x\text{Rh-HNS-1}$ and $\text{MoO}_x\text{Rh-HNS-3}$ (Fig. S1). Without Rh precursor, only a broad peak at 44° was found, which was difficult to index to Mo (JCPDS: PDF#: 42-1120) or MoO_2 (JCPDS: PDF#: 50-0739) / MoO_3 (JCPDS: PDF#: 21-0569). Based on this analysis, MoO_x was defined. To identify the difference in electronic configurations, XPS has been tested (Fig. S2). Mo-O, C-O and OH moieties were composed of O 1s peak for MoO_x shown in Fig. 1b, also underlining the formation of MoO_x . Similarly, O 1s XPS peak was fitted to Rh-O, C-O and OH species at 531.3, 532.4 and 533.1 eV for Rh-HNS [41]. The emergence of Rh-O specie originated from the coordination of oxygen atoms at edge sites [42,43]. In case of $\text{MoO}_x\text{Rh-HNS-2}$, O 1s XPS core level spectrum was deconvoluted into Mo-O, Rh-O, C-O and OH moieties. Moreover, Mo-O peak was negatively shifted compared to the counterpart in MoO_x ; in contrast, Rh-O peak in $\text{MoO}_x\text{Rh-HNS-2}$ located at a higher binding energy by comparison with Rh-HNS . From the O 1s spectra, it was noticed that the introduction of MoO_x into Rh-HNS adjusted the electronic configuration of Rh. Mo atoms were dominant electron donors to oxygen atoms and in electron deficient state; thereby, more metallic Rh was achieved for $\text{MoO}_x\text{Rh-HNS-2}$. As shown in Fig. 1c, the Rh 3d XPS peaks were fitted into metallic Rh and Rh^{3+}

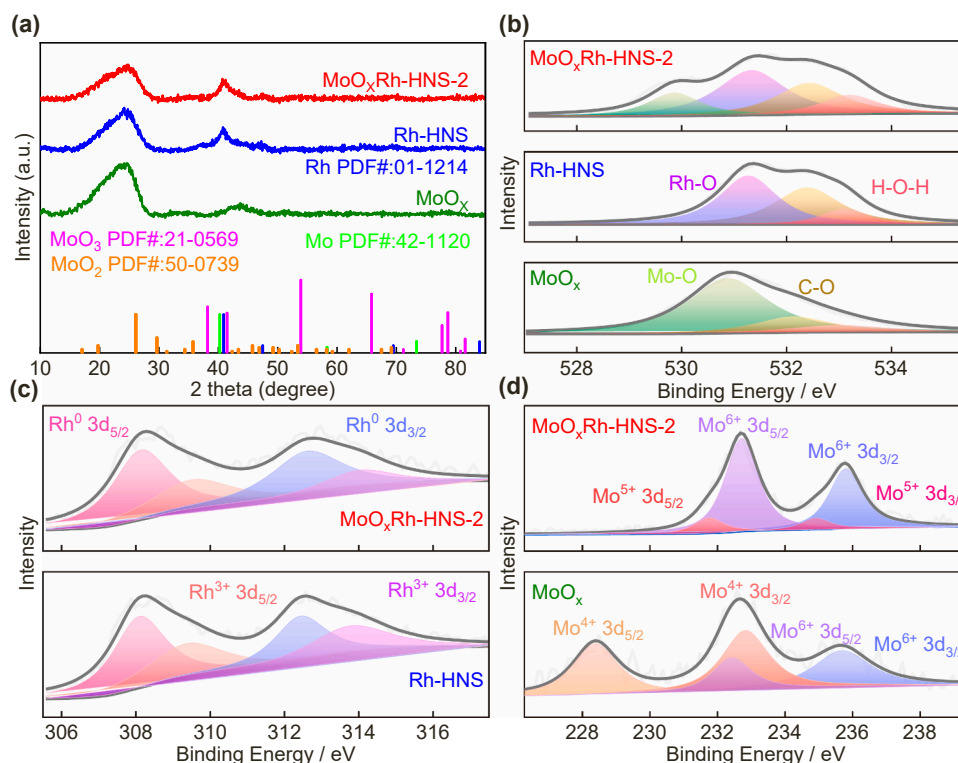


Fig. 1. (a) XRD patterns of $\text{MoO}_x\text{Rh-HNS}$, Rh-HNS and MoO_x . O 1s (b), Rh 3d (c) and Mo 3d (d) XPS spectra of $\text{MoO}_x\text{Rh-HNS-2}$, Rh-HNS and MoO_x .

species for both Rh $3d_{5/2}$ and Rh $3d_{3/2}$ centered at 308.2 and 312.7 eV [44]. Interestingly, the incorporation of MoO_x decreased the percentage of Rh oxides. As analyzed in O 1s spectra, Mo predominantly coordinated with oxygen atoms; therefore, more Rh atoms were in metallic state. Consequently, Mo 3d XPS spectrum of $\text{MoO}_x\text{Rh-HNS-2}$ was fitted to $\text{Mo}^{5+} 3d_{5/2}$, $\text{Mo}^{5+} 3d_{3/2}$, $\text{Mo}^{6+} 3d_{5/2}$ and $\text{Mo}^{6+} 3d_{3/2}$ species at 231.8 eV, 234.9 eV, 232.7 eV and 235.8 eV, respectively (Fig. 1d). Differently, MoO_x was composed of $\text{Mo}^{6+} 3d_{5/2}$ (232.4 eV), $\text{Mo}^{4+} 3d_{5/2}$ (228.4 eV), $\text{Mo}^{6+} 3d_{3/2}$ (235.7 eV) and $\text{Mo}^{4+} 3d_{3/2}$ (232.8 eV), moieties. The XPS spectra of Mo 3d also supported the high valance state of Mo in $\text{MoO}_x\text{Rh-HNS-2}$.

To detect the morphology, SEM test has been conducted. Hierarchical nanosheet structure was observed for pure Rh as displayed in Fig. 2a. With the introduction of MoO_x to Rh, hierarchical nanosheet structure was well maintained (Fig. 2b). With the decrement in MoO_x content, hierarchical nanosheet structure was still observed; however, with the increment in MoO_x percentage, nanosheets aggregated into nanorods ($\text{MoO}_x\text{Rh-HNS-3}$, Fig. S3). Therefore, it was concluded that the Rh was essential for manufacturing the hierarchical nanosheet structure. The structure of Rh-HNS was also underlined by TEM measurement in Fig. 2c. The thickness of nanosheet was determined to 1.7 nm from Fig. 2d. Also, HR-TEM showed distinct a lattice spacing of 0.22 nm

corresponding to (111) facet of metallic Rh. Meanwhile, Fig. 2e confirms the hierarchical nanosheet structure of $\text{MoO}_x\text{Rh-HNS-2}$; also, the thickness of nanosheet was comparable to Rh-HNS. To confirm the thickness of $\text{MoO}_x\text{Rh-HNS-2}$, AFM test has been conducted and the thickness of $\text{MoO}_x\text{Rh-HNS-2}$ was 1.67 nm (Fig. S4), well matched with TEM analysis. HR-TEM image clearly showed the heterointerface between metallic Rh and amorphous MoO_x (Fig. 2f). The HAADF-STEM image and corresponding EDS mapping exhibited the well distribution of Mo, O and Rh elements over the entire structure (Fig. 2g). The overlapped image also underscored the well distribution of Mo and O elements on Rh nanosheets.

3.2. HER performance evaluation

Hydrogen evolution reaction (HER) performance was verified in 1 M KOH. MoO_x exhibited an inferior HER performance to Pt/Rh based electrocatalyst shown in Fig. 3a. Commercial Pt/C with overpotential of 24.7 mV and 386.0 mV to achieve 10 mA cm^{-2} and 200 mA cm^{-2} was recorded. $\text{MoO}_x\text{Rh-HNS-2}$ showed a better HER activity than Rh-HNS with overpotential decreased by 11.5 mV and 102.5 mV at 10 mA cm^{-2} and 200 mA cm^{-2} . The incorporation of MoO_x boosted the alkaline HER activity stemming from the better ability for water

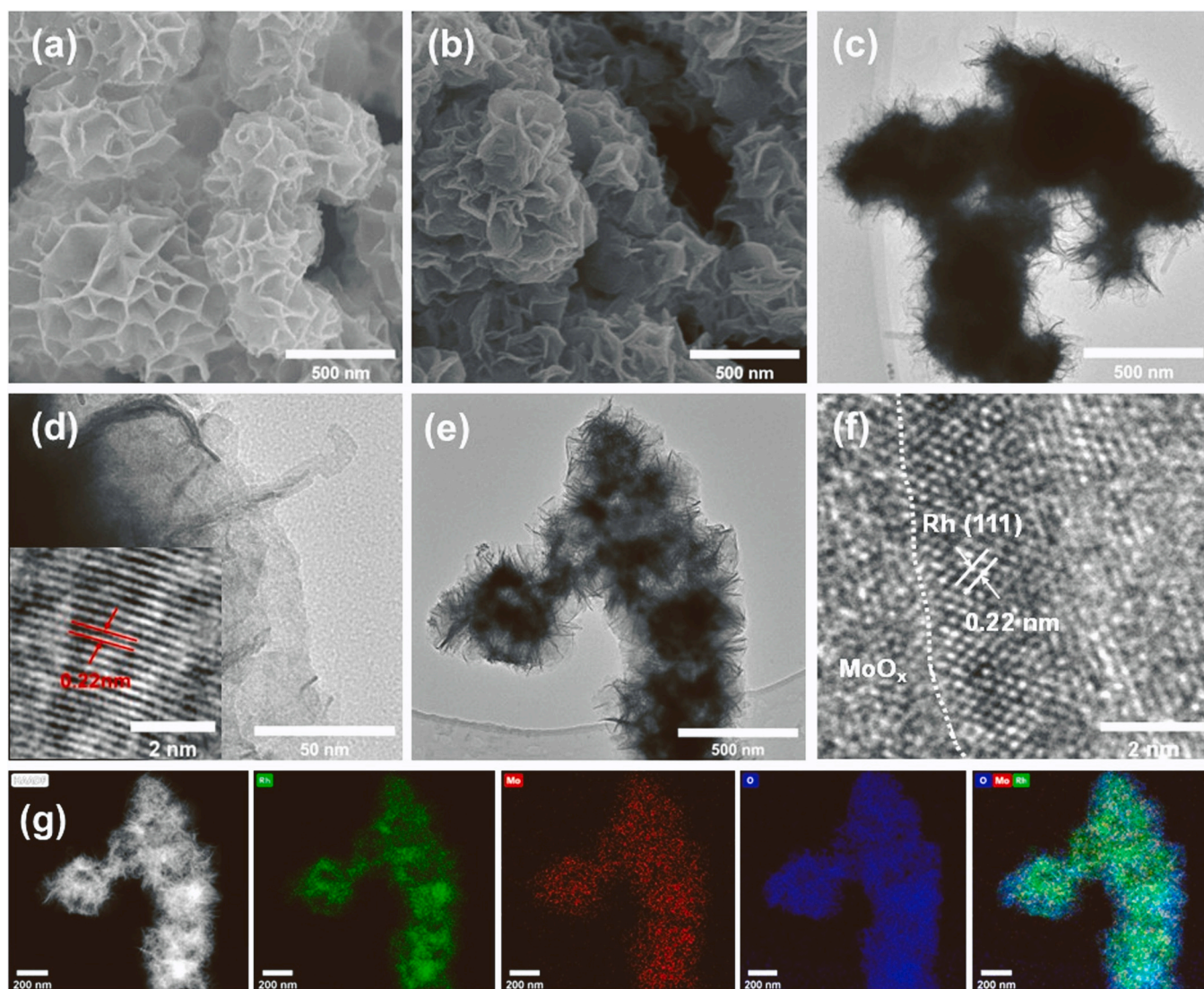


Fig. 2. SEM image of Rh-HNS (a), $\text{MoO}_x\text{Rh-HNS-2}$ (b). TEM images of Rh-HNS (c, d) and $\text{MoO}_x\text{Rh-HNS-2}$ (e, f). (g) HAADF-STEM image and related EDS mapping of $\text{MoO}_x\text{Rh-HNS-2}$.

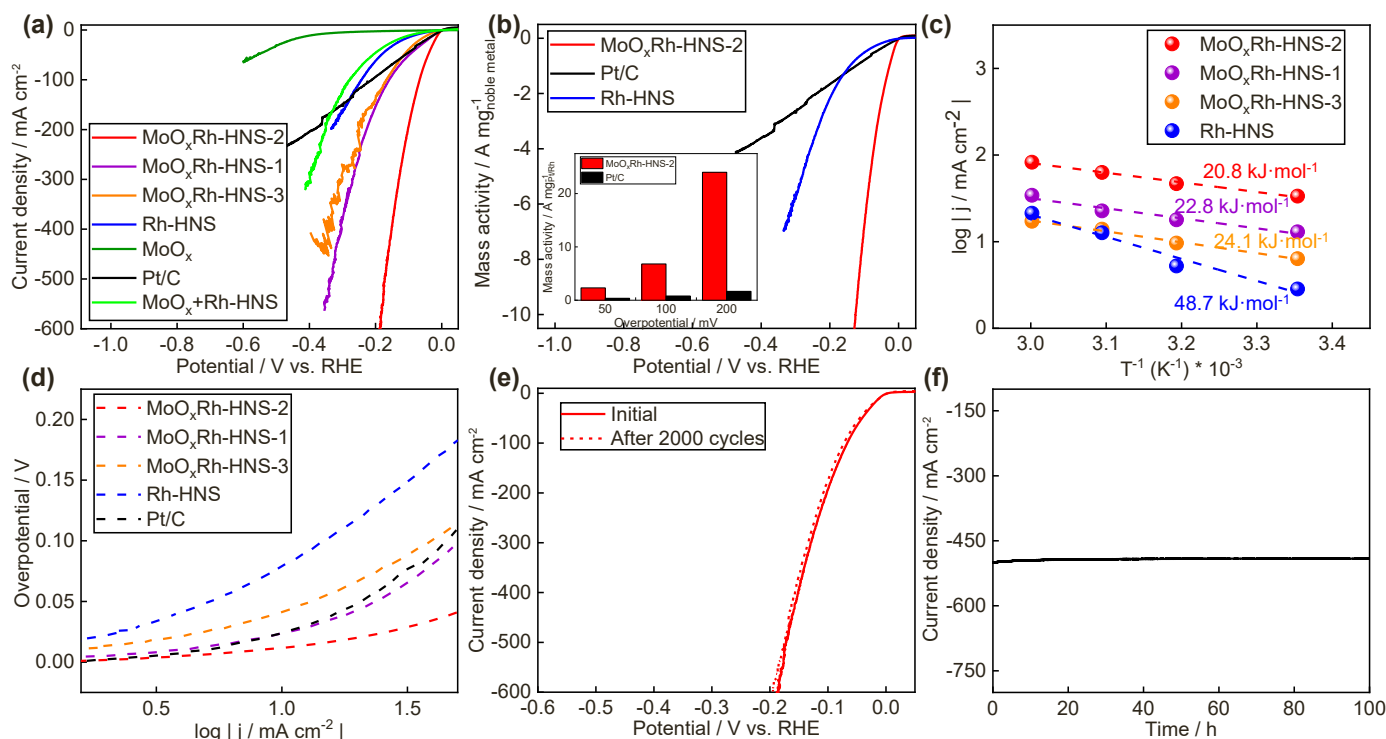


Fig. 3. (a) HER activities of Pt/C, Rh-HNS, MoO_xRh-HNS-1, MoO_xRh-HNS-2, MoO_xRh-HNS-3 and MoO_x. (b) Mass activities of Pt/C, Rh-HNS and MoO_xRh-HNS-2. (c) Activation energies for Rh-HNS, MoO_xRh-HNS-1, MoO_xRh-HNS-2 and MoO_xRh-HNS-3. (d) Tafel slope curves. Cyclic stability (e) and i-t (f) of MoO_xRh-HNS-2.

cleavage (Volmer reaction), highlighted by relatively lower overpotential of MoO_xRh-HNS-1 and MoO_xRh-HNS-3. Moreover, only 185.8 mV overpotential was required to reach 600 mA cm^{-2} for MoO_xRh-HNS-2. Furthermore, MoO_xRh-HNS-2 exhibited a better HER performance than the physically mixed MoO_x and Rh HNS denoted as MoO_x + Rh-HNS highlighting the electronic interaction between MoO_x and Rh at atomic level was important to promote HER catalytic activity. Mass activity of MoO_xRh-HNS-2 was boosted by 6.4 and 8.6 times with relative to Pt/C at overpotential of 50 mV and 100 mV shown in Fig. 3b. The robust HER catalytic activity of MoO_xRh-HNS-2 attributed to the quantitative active sites evidenced by double layer capacitance (C_{dl}) (Fig. S5). MoO_xRh-HNS-2 with a C_{dl} of 27.8 mF cm^{-2} was noticed, which was larger than MoO_xRh-HNS-1 (17.6 mF cm^{-2}), MoO_xRh-HNS-3 (23.9 mF cm^{-2}) and Rh-HNS (14.7 mF cm^{-2} , Fig. S6). As shown in Fig. S7, the introduction of MoO_x to Rh-HNS showed a superior intrinsic HER activity. To confirm this point, turnover frequency (TOF) was evaluated and MoO_xRh-HNS-2 obtained a superior TOF of 17.5 s^{-1} at -50 mV vs. RHE, boosted by 3.4- and 12.5-fold than Pt/C and Rh-HNS (Fig. S8). Also, the charge transfer resistance (R_{ct}) of MoO_xRh-HNS-2 was as low as 30 Ω (Fig. S9), decreased by 4-fold compared to Rh-HNS. To deeply observe the boosted HER performance of MoO_xRh-HNS-2, HER performance was tested under different temperatures (Fig. S10) to estimate the activation energy. As shown in Fig. 3c, the activation energy was dramatically decreased with the incorporation of MoO_x as activation energy for MoO_xRh-HNS-1, MoO_xRh-HNS-2 and MoO_xRh-HNS-3 was 22.8 kJ mol^{-1} , 20.8 kJ mol^{-1} and 24.1 kJ mol^{-1} lower than Rh-HNS (48.7 kJ mol^{-1}), underscoring the significance of MoO_x for promoting the HER catalytic performance. To know the reaction kinetics, Tafel slope was plotted in Fig. 3d, in which 40.4 mV dec^{-1} , 82.8 mV dec^{-1} , 42.4 mV dec^{-1} , 22.5 mV dec^{-1} and 82.8 mV dec^{-1} was calculated for Pt/C, Rh-HNS, MoO_xRh-HNS-1, MoO_xRh-HNS-2 and MoO_xRh-HNS-3, respectively. All electrocatalysts, except MoO_xRh-HNS-2, followed Volmer-Heyrovsky HER mechanism via Tafel slope value [45]. As generally accepted that the theoretical Tafel slope is 30 mV dec^{-1} , 40 mV dec^{-1} and 120 mV dec^{-1} for Tafel, Heyrovsky and Volmer step,

respectively [46]. While, MoO_xRh-HNS-2 with a smaller Tafel slope of 22.5 mV dec^{-1} was recorded, manifesting a different HER mechanism was noticed, as will be discussed below. As shown in Figure Table S1, MoO_xRh-HNS-2 was noticed as one of the most efficiently electrocatalyst toward alkaline HER catalysis. As shown in Fig. 3e, MoO_xRh-HNS-2 exhibited an exceptional cyclic durability with overpotential at 600 mA cm^{-2} upshifted by only 8 mV after 2000 CV cycles attributed to the exceptional structural stability proved by the well-maintained C_{dl} and R_{ct} (Fig. S11). Also, stable current density was recorded for MoO_xRh-HNS-2 at various potentials underlining the superior stability. Moreover, the Tafel slope was similar to initial value suggesting the HER mechanism was remained (Fig. S12). In order to verify the superior structural stability, TEM test has been conducted for MoO_xRh-HNS-2 after i-t test. As shown in Fig. S13, nanosheet structure was still well maintained and the distinct lattice spacing of 0.22 nm also confirmed the presence of Rh (111) facet; in addition, the heterointerface was still distinctly observed. The HAADF-STEM image confirmed the uniform distribution of Mo, O and Rh over the entire architecture. The superior stability was also underlined by the unobvious degradation in HER performance of MoO_xRh-HNS-1 (Fig. S14) and MoO_xRh-HNS-3 (Fig. S15). Contrarily, overpotential at 100 mA cm^{-2} was increased by 58 mV for commercial Pt/C (Fig. S16) ascribing to the Pt aggregation. Similarly, a large decay in HER activity was observed for Rh-HNS due to the more Rh-O bond resulting in fast electrochemical dissolution (Fig. S17). Moreover, the i-t test indicated that MoO_xRh-HNS-2 showed a superior stability with only 3 % decay in performance at 500 mA cm^{-2} during 100 h (Fig. 3f). H₂ was collected by drainage method to calculate the hydrogen yielding rate and a producing rate of 0.1 $\text{mL min}^{-1} \text{cm}^{-2}$ was recorded for MoO_xRh-HNS-1 at -0.1 V vs. RHE, 4.5-fold higher than Pt/C; moreover, the H₂ yield was similar to theoretical value, implying the Faradic efficiency reached 100 % (Fig. S18).

3.3. Confirmation of hydrogen spillover

As displayed in Fig. 3d, Tafel slope of MoO_xRh-HNS-2 suggested a

different HER mechanism by comparison with other electrocatalysts. According to previous reports, hydrogen spillover involving mechanism was noticed for electrocatalyst with Tafel slope lower than 30 mV dec^{-1} [47,48]. To confirm the mechanism, HER performance was tested in KOH electrolyte with various pH (Fig. 4a and Fig. S19). HER performance increased with the increment in pH value. The linear plot of $\log |j|$ @ -30 mV vs. RHE I vs. pH shown in Fig. 4b suggested the reaction order was 0.82, 0.39 and 2.35 for Pt/C, Rh-HNS and $\text{MoO}_x\text{Rh-HNS-2}$, respectively. Reaction order of $\text{MoO}_x\text{Rh-HNS-2}$ was closer to the theoretical value of 2; thereby, the hydrogen spillover involving mechanism was confirmed [49]. To further confirm the hydrogen spillover, CV curves were recorded with different scan rates (Fig. 4c). It was found that the hydrogen desorption peak positively shifted with the increment in scan speed for $\text{MoO}_x\text{Rh-HNS-2}$, Rh-HNS and Pt/C (Fig. S20). Thus, it was reasonable to quantify the kinetics of hydrogen desorption via plotting peak position of hydrogen desorption vs. scan speed (Fig. 4d). The fitted slope was 0.86×10^{-4} , which was almost half of the counterparts for Rh-HNS (1.06×10^{-4}) and Pt/C (1.19×10^{-4}), indicating the fast electro-desorption of hydrogen. It was noticed that the electro-desorption of hydrogen could be accelerated by hydrogen spillover for metal-support electrocatalyst [40]; in this regard, hydrogen spillover was found in $\text{MoO}_x\text{Rh-HNS-2}$. The hydrogen desorption peak of $\text{MoO}_x + \text{Rh-HNS}$ was also positively shifted with the increment in scan rate resulting in a fitting slope of 1.08×10^{-4} (Fig. S21), which was higher than $\text{MoO}_x\text{Rh-HNS-2}$ demonstrating the difficulty in desorption of adsorbed hydrogen for $\text{MoO}_x + \text{Rh-HNS}$ with relative to $\text{MoO}_x\text{Rh-HNS-2}$; therefore, the electronic interplay between Rh and MoO_x was vital for hydrogen spillover to enhance HER performance. Electrochemical impedance spectroscopy (EIS) is a powerful technology to identify the change at electrolyte-electrocatalyst interface with high frequency [50]. Therefore, operando EIS was performed. As shown in Fig. 4e, phase angle decreased with the increment in overpotential at low frequency ($<100 \text{ Hz}$) revealing the HER occurred; while, phase angle was almost the same for Rh-HNS at high frequency ($>100 \text{ Hz}$)

illustrating the electrolyte-electrocatalyst interface was stable [51]. However, with the overpotential increasing, phase angle was also increased in high frequency region ($>100 \text{ Hz}$) for $\text{MoO}_x\text{Rh-HNS-2}$ shown in Fig. 4f manifesting the electrolyte-electrocatalyst interface was changed stemming from the hydrogen spillover from Rh to MoO_x to form MoO_xH . With the introduction of MoO_x , hydrogen spillover was noticed also evidenced by $\text{MoO}_x\text{Rh-HNS-1}$ and $\text{MoO}_x\text{Rh-HNS-3}$ (Fig. S22). Therefore, hydrogen spillover mechanism was found for $\text{MoO}_x\text{Rh-HNS}$ electrocatalyst.

3.4. DFT calculation

To know the boosted HER performance at atomic level, DFT calculation was performed. The structures and the optimized adsorption configurations of HER intermediates on MoO_xRh and $\text{MoO}_x\text{H}_{\text{ads}}\text{-Rh}$ were presented in Fig. S23. Firstly, density of state (DOS) shown in Fig. 5a suggested the incorporation of MoO_x negligibly affected the electric conductivity of Rh. Moreover, the hydrogen spillover could narrow the band gap for MoO_xRh . As shown in Fig. 5b, d band center of MoO_xRh was upshifted by 0.17 eV compared to Rh; therefore, the water adsorption should be enhanced, which was the primary step for alkaline HER catalysis. As experimental results confirmed the hydrogen spillover, it was noticed that d band center of $\text{MoO}_x\text{H-Rh}$ structure was downshifted by comparison with MoO_xRh depicting the water adsorption on $\text{MoO}_x\text{H-Rh}$ was in a more moderate state [52–54]. As shown in Fig. 5c, the free energy for water adsorption and dissociation was calculated. The water splitting was more susceptible to occur on MoO_xRh than Rh suggesting the significance of MoO_x for boosting alkaline HER performance. To evidence the hydrogen spillover promoting HER, a better water dissociation capability was achieved for $\text{MoO}_x\text{H-Rh}$, well matched with HER test. In alkaline HER catalysis, the hydrogen binding strength is also important for HER catalysis. ΔG_{H^*} of $\text{MoO}_x\text{H-Rh}$ was significantly decreased with the increment in hydrogen coverage (Fig. 5d) since more hydrogen would spillover to MoO_x to

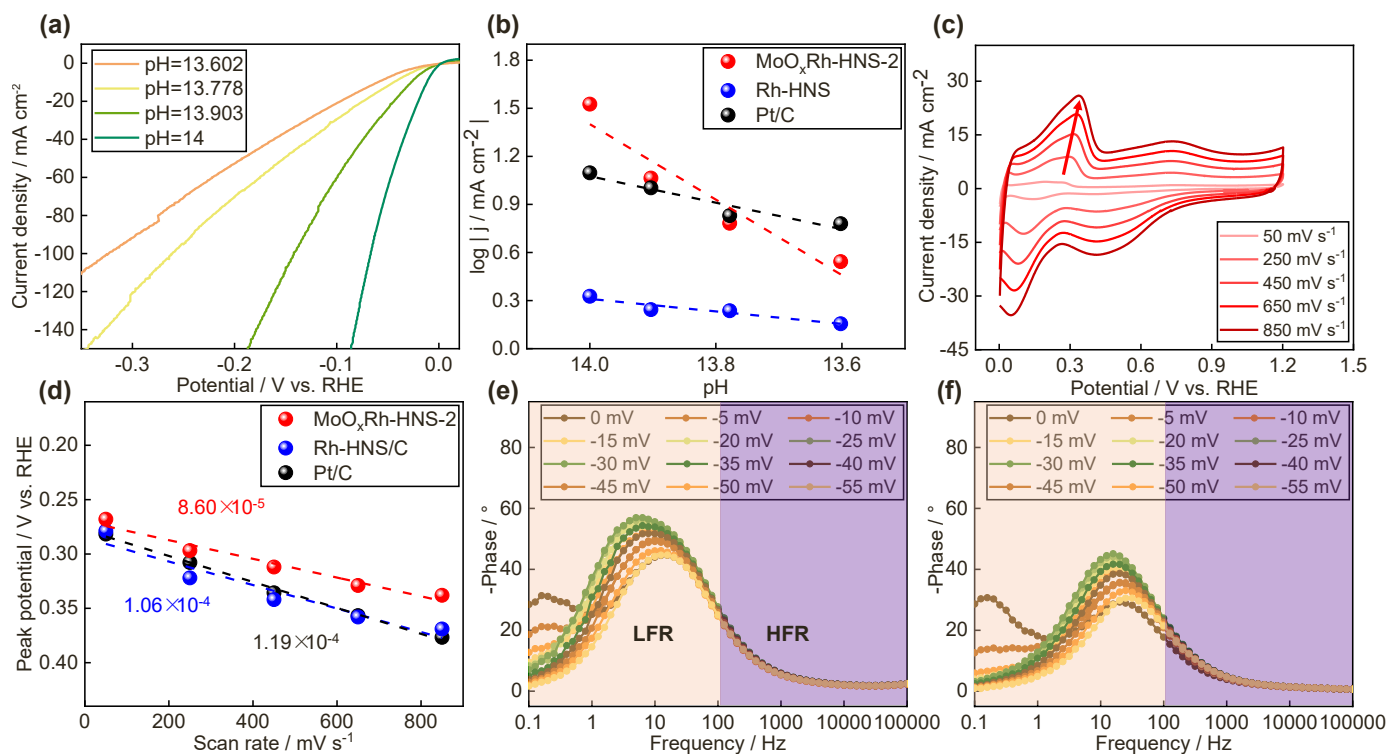


Fig. 4. (a) HER performance of $\text{MoO}_x\text{Rh-HNS-2}$ in KOH electrolyte with various pH. (b) Plots of $\log |j|$ @ -30 mV vs. RHE | vs. pH for Pt/C, Rh-HNS and $\text{MoO}_x\text{Rh-HNS-2}$. (c) Cyclic voltammograms of $\text{MoO}_x\text{Rh-HNS-2}$. (d) The linear plots of peak potentials for Pt/C, Rh-HNS and $\text{MoO}_x\text{Rh-HNS-2}$ vs. scan rates. Phase angles of Rh-HNS (e) and $\text{MoO}_x\text{Rh-HNS-2}$ (f) at various potentials.

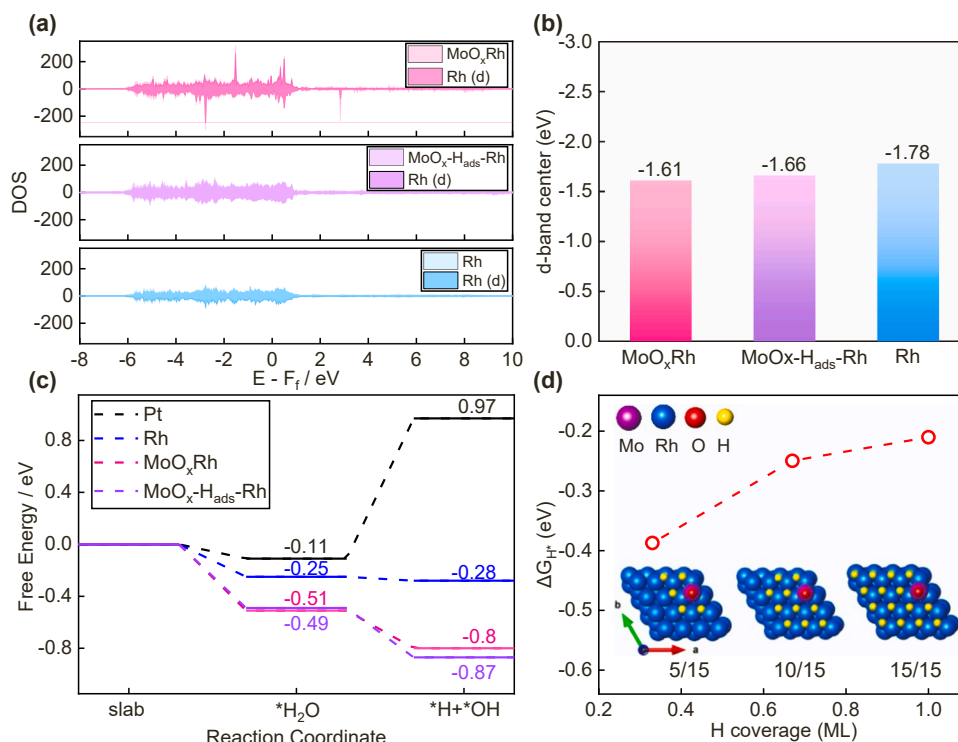


Fig. 5. Density of state (a) and *d* band center (b) of Rh, MoO_xRh and MoO_x-H_{ads}-Rh. (c) Water splitting capability for Pt, Rh, MoO_xRh and MoO_x-H_{ads}-Rh. (d) Gibbs free energies of MoO_x-Rh with different hydrogen coverages.

balance the electro-adsorption/desorption of hydrogen on Rh [55].

4. Conclusions

In this work, we have synthesized rhodium hierarchical nanosheets with molybdenum oxide as atomic dopants (MoO_xRh-HNS). The incorporation of MoO_x reduced the Rh atoms coordinated with oxygen; therefore, an exceptional electrocatalytic performance toward alkaline HER catalysis was achieved for MoO_xRh-HNS demanding only 102.5 mV to attain 200 mA cm⁻², which was lowered by 283.5 mV and 233.5 mV compared to Pt/C and Rh-HNS. Also, the Tafel slope was 22.5 mV dec⁻¹, indicating the hydrogen spillover involving HER mechanism for MoO_xRh-HNS. The hydrogen spillover phenomenon was systematically proved by cyclic voltammetry test, HER activity in various pH and operando electrochemical impedance spectroscopy. Additionally, a robust stability was also recorded for MoO_xRh-HNS with only 3 % degradation at 500 mA cm⁻² during 100 h. Density functional theory calculation suggested the hydrogen atom on MoO_xRh lowered the energy barrier for water dissociation and modulated the hydrogen binding strength to a balanced level.

CRediT authorship contribution statement

Shuyuan Pan: Conceptualization, Data curation **Chen Li:** Data curation **Tiantian Xiong:** Data curation **Yuhua Xie:** Data curation **Fang Luo:** Data curation, Funding acquisition **Zehui Yang:** Conceptualization; Funding acquisition, Supervision; Writing-review & editing.

Declaration of Competing Interest

The authors declare no competing financial interest.

Data Availability

Data will be made available on request.

Acknowledgement

This work is supported by the National Natural Science Foundation of China (No. 22209126).

Appendix A. Supporting information

Supplementary data associated with this article can be found in the online version at [doi:10.1016/j.apcatb.2023.123275](https://doi.org/10.1016/j.apcatb.2023.123275).

References

- [1] F. Luo, Q. Zhang, X. Yu, S. Xiao, Y. Ling, H. Hu, L. Guo, Z. Yang, L. Huang, W. Cai, H. Cheng, Palladium phosphide as a stable and efficient electrocatalyst for overall water splitting, *Angew. Chem. Int. Ed.* 57 (2018) 14862–14867, <https://doi.org/10.1002/anie.201810102>.
- [2] H. Vrubel, D. Merki, X. Hu, Hydrogen evolution catalyzed by MoS₃ and MoS₂ particles, *Energy Environ. Sci.* 5 (2012) 6136–6144, <https://doi.org/10.1039/C2EE02835B>.
- [3] F. Gao, J. He, H. Wang, J. Lin, R. Chen, K. Yi, F. Huang, Z. Lin, M. Wang, Te-mediated electro-driven oxygen evolution reaction, *Nano Res. Energy* 1 (2022) 9120029, <https://doi.org/10.26599/NRE.2022.9120029>.
- [4] Y. Tan, Z. Zhang, Z. Lei, L. Yu, W. Wu, Z. Wang, N. Cheng, Electronic modulation optimizes OH* intermediate adsorption on Co-Nx-C sites via coupling CoNi alloy in hollow carbon nanopolyhedron toward efficient reversible oxygen electrocatalysis, *Appl. Catal. B* 304 (2022), 121006, <https://doi.org/10.1016/j.apcatb.2021.121006>.
- [5] Y. Shi, B. Zhang, Recent advances in transition metal phosphide nanomaterials: synthesis and applications in hydrogen evolution reaction, *Chem. Soc. Rev.* 45 (2016) 1529–1541, <https://doi.org/10.1039/C5CS00434A>.
- [6] F. Luo, H. Hu, X. Zhao, Z. Yang, Q. Zhang, J. Xu, T. Kaneko, Y. Yoshida, C. Zhu, W. Cai, Robust and stable acidic overall water splitting on Ir single atoms, *Nano Lett.* 20 (2020) 2120–2128, <https://doi.org/10.1021/acs.nanolett.0c00127>.
- [7] X. Hu, Y. Li, X. Wei, L. Wang, H. She, J. Huang, Q. Wang, Preparation of double-layered Co–Ni/NiFeOOH co-catalyst for highly meliorated PEC performance in water splitting, *Adv. Powder Mater.* 1 (2022), 100024, <https://doi.org/10.1016/j.apmate.2021.11.010>.
- [8] Z. Pu, J. Zhao, I.S. Amiin, W. Li, M. Wang, D. He, S. Mu, A universal synthesis strategy for P-rich noble metal diphosphide-based electrocatalysts for the hydrogen evolution reaction, *Energy Environ. Sci.* 12 (2019) 952–957, <https://doi.org/10.1039/C9EE00197B>.

- [9] S. Yan, W. Liao, M. Zhong, W. Li, C. Wang, N. Pinna, W. Chen, X. Lu, Partially oxidized ruthenium aerogel as highly active bifunctional electrocatalyst for overall water splitting in both alkaline and acidic media, *Appl. Catal. B* 307 (2022), 121199, <https://doi.org/10.1016/j.apcatb.2022.121199>.
- [10] Y. Yu, S.J. Lee, J. Theerthagiri, Y. Lee, M.Y. Choi, Architecting the AuPt alloys for hydrazine oxidation as an anolyte in fuel cell: comparative analysis of hydrazine splitting and water splitting for energy-saving H₂ generation, *Appl. Catal. B* 316 (2022), 121603, <https://doi.org/10.1016/j.apcatb.2022.121603>.
- [11] Z. Pu, T. Liu, I.S. Amiinu, R. Cheng, P. Wang, C. Zhang, P. Ji, W. Hu, J. Liu, S. Mu, Transition-metal phosphides: activity origin, energy-related electrocatalysis applications, and synthetic strategies, *Adv. Funct. Mater.* 30 (2020) 2004009, <https://doi.org/10.1002/adfm.202004009>.
- [12] J. Sun, W. Xu, C. Lv, L. Zhang, M. Shakouri, Y. Peng, Q. Wang, X. Yang, D. Yuan, M. Huang, Y. Hu, D. Yang, L. Zhang, Co/MoN hetero-interface nanoflake array with enhanced water dissociation capability achieves the Pt-like hydrogen evolution catalytic performance, *Appl. Catal. B* 286 (2021), 119882, <https://doi.org/10.1016/j.apcatb.2021.119882>.
- [13] H. Wang, J. Li, K. Li, Y. Lin, J. Chen, L. Gao, V. Nicolosi, X. Xiao, J.-M. Lee, Transition metal nitrides for electrochemical energy applications, *Chem. Soc. Rev.* 50 (2021) 1354–1390, <https://doi.org/10.1039/D0CS00415D>.
- [14] X. Huang, H. Xu, D. Cao, D. Cheng, Interface construction of P-Substituted MoS₂ as efficient and robust electrocatalyst for alkaline hydrogen evolution reaction, *Nano Energy* 78 (2020), 105253, <https://doi.org/10.1016/j.nanoen.2020.105253>.
- [15] L. Meng, L. Li, Recent research progress on operational stability of metal oxide/sulfide photoanodes in photoelectrochemical cells, *Nano Res. Energy* 1 (2022) 9120020, <https://doi.org/10.26599/NRE.2022.9120020>.
- [16] M. Zeng, Y. Chen, J. Li, H. Xue, R.G. Mendes, J. Liu, T. Zhang, M.H. Rummeli, L. Fu, 2D WC single crystal embedded in graphene for enhancing hydrogen evolution reaction, *Nano Energy* 33 (2017) 356–362, <https://doi.org/10.1016/j.nanoen.2017.01.057>.
- [17] Q. Gao, W. Zhang, Z. Shi, L. Yang, Y. Tang, Structural design and electronic modulation of transition-metal-carbide electrocatalysts toward efficient hydrogen evolution, *Adv. Mater.* 31 (2019) 1802880, <https://doi.org/10.1002/adma.201802880>.
- [18] H. Jing, P. Zhu, X. Zheng, Z. Zhang, D. Wang, Y. Li, Theory-oriented screening and discovery of advanced energy transformation materials in electrocatalysis, *Adv. Powder Mater.* 1 (2022), 100013, <https://doi.org/10.1016/j.apmate.2021.10.004>.
- [19] H. Yin, S. Zhao, K. Zhao, A. Muqit, H. Tang, L. Chang, H. Zhao, Y. Gao, Z. Tang, Ultrathin platinum nanowires grown on single-layered nickel hydroxide with high hydrogen evolution activity, *Nat. Commun.* 6 (2015) 6430, <https://doi.org/10.1038/ncomms7430>.
- [20] Y. Zou, S.A. Kazemi, G. Shi, J. Liu, Y. Yang, N.M. Bedford, K. Fan, Y. Xu, H. Fu, M. Dong, M. Al-Mamun, Y.L. Zhong, H. Yin, Y. Wang, P. Liu, H. Zhao, Ruthenium single-atom modulated Ti₃C₂T_x MXene for efficient alkaline electrocatalytic hydrogen production, *EcoMat* 5 (2023), e12274, <https://doi.org/10.1002/eom2.12274>.
- [21] J. Li, S. Wang, J. Chang, L. Feng, A review of Ni based powder catalyst for urea oxidation in assisting water splitting reaction, *Adv. Powder Mater.* 1 (2022), 100030, <https://doi.org/10.1016/j.apmate.2022.01.003>.
- [22] C. Panda, P.W. Menezes, C. Walter, S. Yao, M.E. Miehlich, V. Gutkin, K. Meyer, M. Driess, From a molecular 2Fe-2Se precursor to a highly efficient iron diselenide electrocatalyst for overall water splitting, *Angew. Chem. Int. Ed.* 56 (2017) 10506–10510, <https://doi.org/10.1002/anie.201706196>.
- [23] K.L. Zhou, Z. Wang, C.B. Han, X. Ke, C. Wang, Y. Jin, Q. Zhang, J. Liu, H. Wang, H. Yan, Platinum single-atom catalyst coupled with transition metal/metal oxide heterostructure for accelerating alkaline hydrogen evolution reaction, *Nat. Commun.* 12 (2021) 3783, <https://doi.org/10.1038/s41467-021-24079-8>.
- [24] J. Li, M.N. Banis, Z. Ren, K.R. Adair, K. Doyle-Davis, D.M. Meira, Y.Z. Finckel, L. Zhang, F. Kong, T.-K. Sham, R. Li, J. Luo, X. Sun, Unveiling the nature of Pt single-atom catalyst during electrocatalytic hydrogen evolution and oxygen reduction reactions, *Small* 17 (2021) 2007245, <https://doi.org/10.1002/smll.202007245>.
- [25] P. Kuang, Y. Wang, B. Zhu, F. Xia, C.-W. Tung, J. Wu, H.M. Chen, J. Yu, Pt single atoms supported on N-doped mesoporous hollow carbon spheres with enhanced electrocatalytic H₂-evolution activity, *Adv. Mater.* 33 (2021) 2008599, <https://doi.org/10.1002/adma.202008599>.
- [26] J. Zhang, G. Ren, D. Li, Q. Kong, Z. Hu, Y. Xu, S. Wang, L. Wang, M. Cao, X. Huang, Interface engineering of snow-like Ru/RuO₂ nanosheets for boosting hydrogen electrocatalysis, *Sci. Bull.* 67 (2022) 2103–2111, <https://doi.org/10.1016/j.scib.2022.10.001>.
- [27] K. Wang, J. Zhou, M. Sun, F. Lin, B. Huang, F. Lv, L. Zeng, Q. Zhang, L. Gu, M. Luo, S. Guo, Cu-Doped Heterointerfaced Ru/RuSe₂ Nanosheets with Optimized H and H₂O Adsorption Boost Hydrogen Evolution Catalysis, *Adv. Mater.*, n/a 2300980, <https://doi.org/10.1002/adma.202300980>.
- [28] S. Tang, Z. Liu, F. Qiu, Q. Liu, Y. Mao, L. Zhang, The active ruthenium (101) crystal plane selectively exposed by in situ metal hyperaccumulation on a living plant for overall water splitting, *Green. Chem.* 24 (2022) 9668–9676, <https://doi.org/10.1039/D2GC03351H>.
- [29] J. Chen, G. Qian, H. Zhang, S. Feng, Y. Mo, L. Luo, S. Yin, PtCo@PtSn heterojunction with high stability/activity for pH-universal H₂ evolution, *Adv. Funct. Mater.* 32 (2022) 2107597, <https://doi.org/10.1002/adfm.202107597>.
- [30] M. Zhang, J. Wang, Y. Zhang, L. Ye, Y. Gong, Ultrafine CoRu alloy nanoparticles in situ embedded in Co₄N porous nanosheets as high-efficient hydrogen evolution electrocatalysts, *Dalton Trans.* 50 (2021) 2973–2980, <https://doi.org/10.1039/D0DT04248J>.
- [31] J. Dai, Y. Zhu, Y. Chen, X. Wen, M. Long, X. Wu, Z. Hu, D. Guan, X. Wang, C. Zhou, Q. Lin, Y. Sun, S.-C. Weng, H. Wang, W. Zhou, Z. Shao, Hydrogen spillover in complex oxide multifunctional sites improves acidic hydrogen evolution electrocatalysis, *Nat. Commun.* 13 (2022) 1189, <https://doi.org/10.1038/s41467-022-28843-2>.
- [32] J. Park, S. Lee, H.-E. Kim, A. Cho, S. Kim, Y. Ye, J.W. Han, H. Lee, J.H. Jang, J. Lee, Investigation of the support effect in atomically dispersed Pt on WO₃-x for utilization of Pt in the hydrogen evolution reaction, *Angew. Chem. Int. Ed.* 58 (2019) 16038–16042, <https://doi.org/10.1002/anie.201908122>.
- [33] L. Zhu, H. Lin, Y. Li, F. Liao, Y. Lifshitz, M. Sheng, S.-T. Lee, M. Shao, A rhodium/silicon co-electrocatalyst design concept to surpass platinum hydrogen evolution activity at high overpotentials, *Nat. Commun.* 7 (2016) 12272, <https://doi.org/10.1038/ncomms12272>.
- [34] Y. Cheng, S. Lu, F. Liao, L. Liu, Y. Li, M. Shao, Rh•MoS₂ nanocomposite catalysts with Pt-like activity for hydrogen evolution reaction, *Adv. Funct. Mater.* 27 (2017) 1700359, <https://doi.org/10.1002/adfm.201700359>.
- [35] J. Li, H.-X. Liu, W. Gou, M. Zhang, Z. Xia, S. Zhang, C.-R. Chang, Y. Ma, Y. Qu, Ethylene-glycol ligand environment facilitates highly efficient hydrogen evolution of Pt/CoP through proton concentration and hydrogen spillover, *Energy Environ. Sci.* 12 (2019) 2298–2304, <https://doi.org/10.1039/C9EE00752K>.
- [36] D. Guan, J. Zhou, Z. Hu, W. Zhou, X. Xu, Y. Zhong, B. Liu, Y. Chen, M. Xu, H.-J. Lin, C.-T. Chen, J.-Q. Wang, Z. Shao, Searching general sufficient-and-necessary conditions for ultrafast hydrogen-evolving electrocatalysis, *Adv. Funct. Mater.* 29 (2019) 1900704, <https://doi.org/10.1002/adfm.201900704>.
- [37] L. Zhang, P.F. Liu, Y.H. Li, M.Y. Zu, X. Li, Z. Jiang, Y. Wang, H. Zhao, H.G. Yang, N-modified NiO surface for superior alkaline hydrogen evolution, *ChemSusChem* 11 (2018) 1020–1024, <https://doi.org/10.1002/cssc.201702371>.
- [38] B.-M. Lee, B.-J. Lee, A comparative study on hydrogen diffusion in amorphous and crystalline metals using a molecular dynamics simulation, *Metall. Mater. Trans. A* 45 (2014) 2906–2915, <https://doi.org/10.1007/s11661-014-2230-4>.
- [39] C. Tang, G. Sun, Y. Liu, Is hydrogen diffusion in amorphous metals non-Arrhenian? *Int. J. Hydrog. Energy* 47 (2022) 9627–9634, <https://doi.org/10.1016/j.ijhydene.2022.01.023>.
- [40] J. Li, J. Hu, M. Zhang, W. Gou, S. Zhang, Z. Chen, Y. Qu, Y. Ma, A fundamental viewpoint on the hydrogen spillover phenomenon of electrocatalytic hydrogen evolution, *Nat. Commun.* 12 (2021) 3502, <https://doi.org/10.1038/s41467-021-23750-4>.
- [41] X. Jiang, H. Jang, S. Liu, Z. Li, M.G. Kim, C. Li, Q. Qin, X. Liu, J. Cho, The heterostructure of Ru₂P/WO₃/NPC synergistically promotes H₂O dissociation for improved hydrogen evolution, *Angew. Chem. Int. Ed.* 60 (2021) 4110–4116, <https://doi.org/10.1002/anie.202014411>.
- [42] J. Sun, P. Peng, Y. Xie, X. Yu, K. Qu, L. Peng, H. Bao, F. Luo, Z. Yang, Co single atoms and Co nanoparticle relay electrocatalyst for rechargeable zinc air batteries, *Appl. Catal. B* 319 (2022), 121905, <https://doi.org/10.1016/j.apcatb.2022.121905>.
- [43] C. Li, R. Xu, S. Ma, Y. Xie, K. Qu, H. Bao, W. Cai, Z. Yang, Sulfur vacancies in ultrathin cobalt sulfide nanoflowers enable boosted electrocatalytic activity of nitrogen reduction reaction, *Chem. Eng. J.* 415 (2021), 129018, <https://doi.org/10.1016/j.cej.2021.129018>.
- [44] F. Luo, L. Guo, Y. Xie, J. Xu, W. Cai, K. Qu, Z. Yang, Robust hydrogen evolution reaction activity catalyzed by ultrasmall Rh–Rh₂P₂ Nanopart. *J. Mater. Chem. A* 8 (2020) 12378–12384, <https://doi.org/10.1039/D0TA04773B>.
- [45] H. Li, K. Liu, J. Fu, K. Chen, K. Yang, Y. Lin, B. Yang, Q. Wang, H. Pan, Z. Cai, H. Li, M. Cao, J. Hu, Y.-R. Lu, T.-S. Chan, E. Cortés, A. Fratolocchi, M. Liu, Paired Ru–O–Mo ensemble for efficient and stable alkaline hydrogen evolution reaction, *Nano Energy* 82 (2021), 105767, <https://doi.org/10.1016/j.nanoen.2021.105767>.
- [46] Y. Cheng, X. Fan, F. Liao, S. Lu, Y. Li, L. Liu, Y. Li, H. Lin, M. Shao, S.-T. Lee, Os/Si nanocomposites as excellent hydrogen evolution electrocatalysts with thermodynamically more favorable hydrogen adsorption free energy than platinum, *Nano Energy* 39 (2017) 284–290, <https://doi.org/10.1016/j.nanoen.2017.07.009>.
- [47] Y.-N. Zhou, X. Liu, C.-J. Yu, B. Dong, G.-Q. Han, H.-J. Liu, R.-Q. Lv, B. Liu, Y.-M. Chai, Boosting hydrogen evolution through hydrogen spillover promoted by Co-based, Support Eff., *J. Mater. Chem. A* 11 (2023) 6945–6951, <https://doi.org/10.1039/D2TA09784B>.
- [48] H. Xu, J. Li, X. Chu, Intensifying hydrogen spillover for boosting electrocatalytic hydrogen evolution reaction, *Chem. Rec.* 23 (2023), e202200244, <https://doi.org/10.1002/tcr.202200244>.
- [49] M. Sheng, B. Jiang, B. Wu, F. Liao, X. Fan, H. Lin, Y. Li, Y. Lifshitz, S.-T. Lee, M. Shao, Approaching the volcano top: iridium/silicon nanocomposites as efficient electrocatalysts for the hydrogen evolution reaction, *ACS Nano* 13 (2019) 2786–2794, <https://doi.org/10.1021/acs.nano.8b07572>.
- [50] S. Wang, J. Zhang, O. Gharbi, V. Vivier, M. Gao, M.E. Orazem, Electrochemical impedance spectroscopy, *Nat. Rev. Methods Prim.* 1 (2021) 41, <https://doi.org/10.1038/s43586-021-00039-w>.
- [51] C. Xie, W. Chen, S. Du, D. Yan, Y. Zhang, J. Chen, B. Liu, S. Wang, In-situ phase transition of WO₃ boosting electron and hydrogen transfer for enhancing hydrogen evolution on Pt, *Nano Energy* 71 (2020), 104653, <https://doi.org/10.1016/j.nanoen.2020.104653>.
- [52] Z. Pu, I.S. Amiinu, Z. Kou, W. Li, S. Mu, RuP₂-based catalysts with platinum-like activity and higher durability for the hydrogen evolution reaction at all pH values, *Angew. Chem. Int. Ed.* 56 (2017) 11559–11564, <https://doi.org/10.1002/anie.201704911>.
- [53] C. Li, Y. Yu, M. Li, Z. Yang, F. Luo, Multiple p-d hybridizations in Fe₂P–CoFe₂O₄ heteronanoshells boost the electrocatalytic performance for alkaline water

- splitting, *Int. J. Hydrog. Energy* (2023), <https://doi.org/10.1016/j.ijhydene.2023.06.066>.
- [54] C. Chang, Y. Xie, F. Luo, S. Zhou, Z. Yang, Weakening s-d orbital hybridization of metallic iridium by tungsten atoms for acidic water splitting, *Appl. Catal. A* 649 (2023), 118941, <https://doi.org/10.1016/j.apcata.2022.118941>.
- [55] A.J. Shih, M.C.O. Monteiro, F. Dattila, D. Pavesi, M. Philips, A.H.M. da Silva, R. E. Vos, K. Ojha, S. Park, O. van der Heijden, G. Marcandalli, A. Goyal, M. Villalba, X. Chen, G.T.K.K. Gunasooriya, I. McCrum, R. Mom, N. López, M.T.M. Koper, Water electrolysis, *Nat. Rev. Methods Prim.* 2 (2022) 84, <https://doi.org/10.1038/s43586-022-00164-0>.